

CO-CHANGES II: spatially resolved IRAM 30m CO line observations of 23 nearby edge-on spiral galaxies

Yan Jiang^{1,2}, Jiang-Tao Li¹*, Qing-Hua Tan¹, Li Ji^{1,3}, Joel N. Bregman⁴, Q. Daniel Wang⁵, Jian-Fa Wang^{1,2}, Li-Yuan Lu^{6,1}, and Xue-Jian Jiang⁷

¹ Purple Mountain Observatory, Chinese Academy of Sciences, 10 Yuanhua Road, Nanjing 210023, China

² School of Astronomy and Space Sciences, University of Science and Technology of China, Hefei 230026, China

³ Key Laboratory of Dark Matter and Space Astronomy, CAS, Nanjing 210023, China

⁴ Department of Astronomy, University of Michigan, 311 West Hall, 1085 S. University Ave, Ann Arbor, MI, 48109-1107, U.S.A.

⁵ Department of Astronomy, University of Massachusetts, Amherst, MA 01003, U.S.A.

⁶ Department of Astronomy, Xiamen University, 422 Siming South Road, Xiamen 361005, China

⁷ Research Center for Intelligent Computing Platforms, Zhejiang Laboratory, Hangzhou 311100, China

December 16, 2024

ABSTRACT

Context. Molecular gas, serving as the fuel for star formation, and its relationship with atomic gas are crucial for understanding how galaxies regulate their star forming (SF) activities.

Aims. We conduct IRAM 30m observations of 23 nearby spiral galaxies as part of the CHANG-ES (Continuum Halos in Nearby Galaxies – an EVLA Survey) project to investigate the distribution of molecular gas and the Kennicutt–Schmidt SF law in these galaxies. By combining these results with atomic gas masses studied in previous work, we aim to investigate the scaling relations that connect the molecular and atomic gas masses with stellar masses and the baryonic Tully-Fisher relation.

Methods. Based on spatially resolved observations of the $^{12}\text{CO } J = 1 - 0$, $^{13}\text{CO } J = 1 - 0$, and $^{12}\text{CO } J = 2 - 1$ molecular lines, we calculate the total molecular gas masses, the ratios between different CO lines, and derive some key physical parameters such as the temperature and optical depth of the molecular gas.

Results. The median values of the line ratios $^{12}\text{CO}/^{13}\text{CO } J = 1 - 0$ and $^{12}\text{CO } J = 2 - 1/J = 1 - 0$ are 8.6/6.1 and 0.53/0.39 for the nuclear/disk regions, respectively. The molecular gas mass derived from $^{13}\text{CO } J = 1 - 0$ is strongly correlated with, but systematically lower than, that derived from $^{12}\text{CO } J = 1 - 0$. Most of the galaxies in our sample follow the spatially resolved SF scaling relation between the star formation rate surface density and molecular gas mass surface density, with a median gas depletion timescale of ~ 1 Gyr. A few galaxies exhibit enhanced SF efficiency, with shorter timescales of ~ 0.1 Gyr. Our sample shows a weak correlation between molecular and atomic gas, but a strong correlation between the molecular-to-atomic gas mass ratio ($M_{\text{H}_2}/M_{\text{HI}}$) and stellar mass, consistent with previous studies. Galaxies with lower stellar masses in our sample exhibit an excess of atomic gas by one magnitude compared to molecular gas, suggesting that the transformation of atomic gas into molecular gas is less efficient. Most galaxies tightly follow the baryonic Tully-Fisher relation, but NGC 2992 and NGC 4594 deviate from the relation due to different physical factors. We find that the ratio of the cold gas (comprising molecular and atomic gas) to the total baryon mass decreases with the gravitational potential of the galaxy, as traced by rotation velocity, which could be due to gas consumption in SF or being heated to the hot phase.

Key words. galaxies: ISM - galaxies: spiral - galaxies: star formation - ISM: molecules

1. Introduction

Molecular gas clouds serve as the cradles of stars, with their distribution being closely related to the star formation rate (SFR). Kennicutt (1998) and Schmidt (1959) proposed that regions with higher density of total neutral hydrogen gas ($\text{H}_2 + \text{HI}$) correlate with higher SFR. However, studies focusing on the resolved Kennicutt–Schmidt SF law (SFL) reveal that the SFR primarily follows a strong relationship with molecular gas surface density, all existing within a relatively smooth HI distribution (e.g., Leroy et al. 2008; Bigiel et al. 2008).

Molecular and atomic gas content varies across galaxies and is related to stellar mass, morphology, SFR, stellar surface density and color ($NUV - r$ or $g - r$) (e.g., Saintonge et al. 2011; Saintonge & Catinella 2022; Tacconi et al. 2020). The gas content is usually expressed in terms of the molecular gas mass to stellar mass ($M_{\text{H}_2}/M_{\text{star}}$), atomic gas mass to stellar mass ($M_{\text{HI}}/M_{\text{star}}$), and $M_{\text{H}_2}/M_{\text{HI}}$. Statistical studies based on single-pointing observations of galaxy samples have revealed that the $M_{\text{H}_2}/M_{\text{HI}}$ increases gradually with the M_{\star} (e.g., Saintonge et al. 2017; Boselli et al. 2014; Bothwell et al. 2014; Cicone et al. 2017). Additionally, the study by Catinella et al. (2018) highlighted that changes in $M_{\text{H}_2}/M_{\text{HI}}$ in main-sequence galaxies are primarily driven by variations in the HI reservoir and also

* Corresponding author: pandataotao@gmail.com

confirmed the significance of different galaxy structures on $M_{\text{H}_2}/M_{\text{HI}}$ changes. The proportion of these cold baryonic components may vary across different galaxies. The multi-wavelength data in our sample provide an opportunity for further investigation.

Our project builds on the CHANG-ES project, which involves systematic VLA observations of 35 nearby edge-on spiral galaxies to investigate the relationship between radio coronas, galactic disks, and galactic environments (e.g., Irwin et al. 2012, 2024). In addition to high-resolution multi-band VLA observations, these galaxies also have spatially-resolved data across multi wavelengths. For instance, combining new $\text{H}\alpha$ images with WISE 22 μm data provides more reliable estimates of the SFR for the sample (e.g., Wiegert et al. 2015; Vargas et al. 2019). The subsequent spatially resolved $\text{H}\alpha$ spectral observations are being conducted (e.g., Lu et al. (2024); Li et al. (2024)). High resolution images of HI are obtained by subtracting the continuum emission from VLA L band observations (e.g., Zheng et al. 2022), which provide the distribution and proportion of atomic gases. Some well-known galaxies in this sample have already been observed and analyzed the molecular gas in many literatures, such as NGC 660 (e.g., Israel 2009b), NGC 891 (e.g., Yim et al. 2011), and NGC 3079 (e.g., Irwin & Sofue 1992; Israel 2009a). The remaining galaxies either lack observations or have only single-pointing observations of their galactic nuclei. To enhance our understanding of the distribution and properties of molecular gas, its correlation with SFR, its contribution to the baryonic gas budget, and its interactions with the galactic halo, it is essential to conduct spatially resolved observations and analyses of molecular gas across this sample.

We conduct the CO-CHANGES project, which simultaneously cover the $^{12}\text{CO } J = 1 - 0$, $^{13}\text{CO } J = 1 - 0$ and $^{12}\text{CO } J = 2 - 1$ emission lines, using the IRAM 30m telescope. The $^{12}\text{CO } J = 1 - 0$ line ($T_{\text{ex}} \sim 10$ K; $n_{\text{cir}} \sim 300 \text{ cm}^{-3}$) (Evans 1999) is the best tracer of molecular gas. By combining the three emission lines, we can calculate and analyze the distribution of H_2 gas related to star formation and its physical properties, such as temperature and optical depth (e.g., Frerking et al. 1982; Wilson et al. 2013), which vary across different SF environments, including the nucleus and the disk. These observations are made at selected positions along the galactic disk of 23 out of the 35 CHANG-ES galaxies, including NGC 4594, which is analyzed as a case study in CO-CHANGES Paper I (Jiang et al. 2024). Table 1 lists the CO-CHANGES sample galaxies along with the relevant parameters from previous studies of the CHANG-ES project (e.g., Irwin et al. 2012; Wiegert et al. 2015; Li et al. 2016a; Vargas et al. 2019) which are referenced in this paper. When deriving physical parameters such as the molecular gas temperature and optical depth, we adopt the assumptions and formulas from Paper I, except where deviations are explicitly discussed.

In this paper, we will introduce the IRAM 30m observation and data reduction in Sect. 2, and present the main results in Sect. 3. In Sect. 4, we will discuss the correlation analysis of molecular gas, atomic gas, and stellar mass within the sample, as well as the SFR and the gas baryon budget. Finally, we will summarize the major conclusions in Sect. 5. We note that 3σ threshold is used to determine whether the spectrum is detected, and the errors drawn in the figure are quoted at 1σ level throughout the paper.

2. Observations and Data Reduction

2.1. IRAM 30m observations

We conducted IRAM 30m CO line observations of 23 CHANG-ES galaxies in a few observation runs from August 2018 to March 2019 through the project 063-18 and 189-18 (PI: Jiang-Tao Li). Details of the observations were summarized in Table 2. The observations were taken with the Eight MIXer Receiver (EMIR), with the E90/E230 combination (Carter et al. 2012), which simultaneously covers the $^{12}\text{CO } J = 1 - 0$, $J = 2 - 1$, and $^{13}\text{CO } J = 1 - 0$ lines. The Superconductor-Insulator-Superconductor (SIS) receivers were used for observations in position switching (PSW) mode, with a minimum offset of the reference position from the source position of $122''$. We used the 24 Fourier Transform Spectrometer (FTS) units as backend, covering a total of 32 GHz bandwidth across all channels with a frequency resolution of 200 kHz. The full width at half-maximum (FWHM) of the primary beam of IRAM 30m was $\approx 21.4''$ and $\approx 10.7''$ at 115 GHz and 230 GHz, while the main beam efficiency was set to 78 percent and 59 percent at these frequencies, respectively.¹

We observed 3 to 13 separate positions typically along the disk of each galaxy, in order to study the spatial distribution of the gas. Since most galaxies in our sample are axisymmetric, we can position the beams asymmetrically around the galaxy center, increasing the number of sampling points on one side, which facilitates subsequent kinematic analyses, such as rotation curve fitting. One of these observations in each galaxy is pointed at the galaxy nucleus. Refer to the appendix for the specific distribution of the observation positions. The on-source integration time for most of these positions was 9.8 minutes, while for outer regions of disk we doubled the on-source integration time to increase the signal-to-noise ratio (S/N). The total integration time for all galaxies amounted to 56 hours.

2.2. Data reduction

We utilized the CLASS (Continuum and Line Analysis Single-dish software) from the GILDAS package (version jul21)² to reduce and analyze the IRAM 30m/EMIR data. In CO-CHANGES Paper I, we used an older version (jan17a) for NGC 4594, which did not result in significant differences.

Data taken with the FTS backend sometimes showed intermittent ‘‘platforming’’ issues between individual units³. Following the methodology outlined in CO-CHANGES Paper I (see also Lisenfeld et al. (2019)), we corrected the ‘‘platforming’’ issues and binned the $^{12}\text{CO } J = 1 - 0$, $J = 2 - 1$, and $^{13}\text{CO } J = 1 - 0$ spectra to a resolution of $\Delta v = 10 \text{ km s}^{-1}$ for all galaxies. Different from the Paper I, we primarily fitted spectra using a polynomial function of up to the second degree. To combine the spectra from different polarization components and multiple on-source integration times, we used sigma-weighted averaging.

Approximately 22% of the $^{12}\text{CO } J = 2 - 1$ spectra were affected by standing waves, mainly from horizontal polar-

¹ <http://www.iram.es/IRAMES/mainWiki/Iram30mEfficiencies>

² <http://www.iram.fr/IRAMFR/GILDAS>

³ <https://www.iram.fr/~gildas/demos/class/class-tutorial.pdf>

Table 1. Parameters of the sample galaxies.

Name	Distance	TC	V_{rot}	Diameter	M_{\star}	M_{HI}	SFR	Σ_{SFR}
(1)	(Mpc)	(3)	(km s^{-1})	(kpc)	($\times 10^{10} M_{\odot}$)	($\times 10^{10} M_{\odot}$)	($M_{\odot} \text{ yr}^{-1}$)	($\times 10^{-3} M_{\odot} \text{ yr}^{-1} \text{ kpc}^{-2}$)
(1)	(2)	(3)	(4)	(5)	(6)	(7)	(8)	(9)
NGC2613	23.4	3.0 ± 0.3	290.6	33.7	12.0 ± 0.2	0.712^a	3.36 ± 0.35	3.77 ± 0.39
NGC2683	6.27	3.0 ± 0.3	202.6	9.39	1.49 ± 0.02	0.052^b	0.25 ± 0.03	3.54 ± 0.40
NGC2820	26.5	5.0 ± 0.5	162.8	13.8	0.467 ± 0.013	1.424^c	1.35 ± 0.14	9.00 ± 0.96
NGC2992	34.0	1.0 ± 0.3	58.7	12.5	5.26 ± 0.09	0.738^d	5.91 ± 0.54	48.2 ± 4.4
NGC3003	25.4	4.0 ± 0.6	120.6	27.7	0.485 ± 0.010	1.072^b	1.56 ± 0.16	2.59 ± 0.27
NGC3044	20.3	5.0 ± 0.5	152.6	18.1	0.660 ± 0.013	0.363^b	1.75 ± 0.16	6.79 ± 0.60
NGC3432	9.42	9.0 ± 0.3	109.9	9.96	0.100 ± 0.002	0.222^c	0.51 ± 0.06	6.36 ± 0.69
NGC3448	24.5	5.0 ± 0.0	119.5	12.5	0.564 ± 0.011	0.832^b	1.78 ± 0.18	14.5 ± 1.5
NGC3556	14.1	6.0 ± 0.3	153.2	24.9	2.81 ± 0.04	0.479^b	3.57 ± 0.30	7.32 ± 0.62
NGC3735	42.0	5.0 ± 0.5	241.1	34.4	14.9 ± 0.2	1.160^c	6.23 ± 0.57	6.71 ± 0.61
NGC3877	17.7	5.0 ± 0.3	155.1	18.5	2.74 ± 0.04	0.148^b	1.35 ± 0.12	5.04 ± 0.44
NGC4096	10.3	5.0 ± 0.3	144.8	11.8	0.613 ± 0.010	0.145^b	0.71 ± 0.08	6.52 ± 0.77
NGC4157	15.6	3.0 ± 0.5	188.9	16.6	2.92 ± 0.04	0.525^b	1.76 ± 0.18	8.15 ± 0.83
NGC4217	20.6	3.0 ± 0.3	187.6	23.4	4.74 ± 0.07	0.275^b	1.89 ± 0.18	4.40 ± 0.42
NGC4244	4.40	6.0 ± 0.3	97.8	14.8	0.090 ± 0.002	0.067^c	0.06 ± 0.01	0.37 ± 0.04
NGC4302	19.4	5.0 ± 0.5	167.4	3.82	3.43 ± 0.05	0.174^b	0.92 ± 0.08	2.52 ± 0.21
NGC4594	12.7	1.0 ± 0.3	408.0	22.0	26.1 ± 0.4	0.033^c	0.43 ± 0.04	1.14 ± 0.10
NGC4666	27.5	5.0 ± 0.3	192.9	32.3	12.5 ± 0.2	1.096^b	10.5 ± 0.9	12.8 ± 1.1
NGC4845	17.0	2.0 ± 0.3	176.0	10.4	2.89 ± 0.05	0.009^c	0.62 ± 0.06	7.33 ± 0.68
NGC5084	23.4	-2.0 ± 0.3	312.9	4.99	12.3 ± 0.2	0.912^b	–	–
NGC5297	40.4	4.5 ± 0.5	189.5	25.9	3.69 ± 0.07	1.992^e	3.00 ± 0.33	5.70 ± 0.62
NGC5792	31.7	3.0 ± 0.3	208.6	23.7	8.89 ± 0.16	1.413^b	4.41 ± 0.37	10.0 ± 0.8
UGC10288	34.1	5.3 ± 0.6	167.1	21.3	2.03 ± 0.05	0.955^b	0.66 ± 0.07	1.85 ± 0.21

Notes. Galaxy parameters. (1) Galaxy name. (2) Distance is obtained from Vargas et al. (2019). (3) TC, the morphological type code from de Vaucouleurs et al. (1991), except for NGC 3448, which is from Huchra et al. (2012). (4) V_{rot} is the maximum atomic gas rotation velocity corrected for inclination obtained from HyperLeda (<http://leda.univ-lyon1.fr/>), as also noted in Makarov et al. (2014). (5) Diameter is derived from 22 μm data by Wiegert et al. (2015). (6) M_{\star} is the stellar mass from Li et al. (2016a), which is derived from the *2MASS* *K*-band apparent magnitude (Skrutskie et al. 2006). (7) M_{HI} , the total atomic gas mass, is directly available for 14 galaxies from Zheng et al. (2022). The source of the H I flux is indicated by superscript, and the detailed calculation methods are summarized in Sect. 4.1. References and corresponding observational instruments are as follows: a. Chaves & Irwin (2001) with VLA L-band CnB-array; b. Zheng et al. (2022) with VLA L-band C-array; c. Courtois & Tully (2015), who uniformly processed data from various telescope (NGC 2820 and NGC 3735 from Green Bank 42m; NGC 3432, NGC 4244 and NGC 4594 from Robert C. Byrd Green Bank Telescope; NGC 4845 from Arecibo with line feed system.); d. Huchtmeier (1982) with NRAO 91m; e. Davis & Seaquist (1983) with NRAO 91m. (8) SFR is the revised star formation rate from Vargas et al. (2019), calculated using a combination of H α and 22 μm data. (9) Σ_{SFR} is the surface density of SFR and calculated using the 22 μm diameter and obtained from Vargas et al. (2019).

ization. For spectra with $S/N > 7\sigma$, we retained the data without correction. For spectra with $3\sigma < S/N < 7\sigma$, we subtracted a sinusoidal function based on conditions from other polarization or observations. This correction, applied to only 1% of the data, was made when it did not significantly affect the signal and indeed improved the rms. We excluded spectra with $S/N < 3\sigma$ affected by standing waves, accounting for 11% of the total $^{12}\text{CO } J = 2 - 1$ spectra. The rms thresholds varied for each galaxy, with an average of 30 mK. This exclusion typically reduced the rms from approximately 40 mK to 10 mK.

For $^{12}\text{CO } J = 1 - 0$ and $^{13}\text{CO } J = 1 - 0$ spectra, all data were retained except for NGC 3735, in which the $^{13}\text{CO } J = 1 - 0$ spectra at positions “1” to “4” were not covered due to the incorrect frequency settings during observations on August 24, 2018.

Unexpected spike features were detected in some spectra, which could affect the analysis of the emission lines. For example, in the $^{13}\text{CO } J = 1 - 0$ and $^{12}\text{CO } J = 2 - 1$ spectra of NGC 2613 and NGC 3044, we observed abnormal spikes at fixed rest frequencies that do not shift with redshift, as shown in Fig. 1 within the velocity range indicated by the blue box. In NGC 3044, these spikes were

Table 2. IRAM 30m observation log.

Galaxy	RA	DEC	Date	$\tau_{225\text{GHz}}$	n_{obs}	t_{exp}	t_{exp}	t_{exp}	rms	rms	rms
	(J2000)	(J2000)				(min)	(min)	(min)	(mk)	(mk)	(mk)
(1)	(2)	(3)	(4)	(5)	(6)	(7)	(8)	(9)	(10)	(11)	(12)
NGC2613-1	8:33:18.39	-22:57:56.73	2/25/2019	0.26	1	19.63	19.63	19.63	15.48	6.71	16.21
NGC2613-2	8:33:21.30	-22:58:15.54	2/25/2019	0.26	1	19.63	19.63	19.63	14.94	4.99	10.71
NGC2613-3	8:33:22.75	-22:58:24.95	2/25/2019	0.26	1	19.63	19.63	19.63	14.54	5.05	10.92
...				

Notes. Listed items (The full version is only available online.): (1) Galaxy name with observation positions. Bold names indicate companion galaxy or non-disk position (possibly halfway to the companion galaxy), with companion galaxies indicated in parentheses. (2) Position RA. (3) Position DEC. (4) Observation date. (5) $\tau_{225\text{GHz}}$ is the average opacity at 225 GHz during observation dates. (6) n_{obs} is the total number of observation scans at each position, with each scan having an effective on-source integration time of 9.8 minutes. (7)-(9) The total on-source integration time at each position for $^{12}\text{CO } J = 1 - 0$, $^{13}\text{CO } J = 1 - 0$, and $^{12}\text{CO } J = 2 - 1$ lines, respectively, including both vertical and horizontal polarization components. (10)-(12) The root mean square (rms), calculated from fitting the baseline of the combined spectra for both polarization components for $^{12}\text{CO } J = 1 - 0$, $^{13}\text{CO } J = 1 - 0$, and $^{12}\text{CO } J = 2 - 1$ lines, respectively.

only detected on specific dates. We therefore attributed these signals to RFI (Radio Frequency Interference) and subsequently masked these spikes. However, for NGC 2613 at positions “2”, “3”, and “4”, the spikes were mixed with the galactic $^{13}\text{CO } J = 1 - 0$ lines and could not be easily masked. Hence, we applied a Gaussian fit (the blue curve in Fig. 1) to the spike at position “1”, fixing its line width and intensity, to subtract the spikes from the other three positions (“2”, “3”, and “4”). We applied 3σ to these three positions and excluded them from the statistical analysis. The fitting results were presented in Table 3. For the remaining galaxies, we did not correct for RFI as it did no affect on the lines of interest.

In our sample, five galaxies exhibited $^{12}\text{CO } J = 1 - 0$ emission in their nuclei with a total velocity width exceeding 400 km s^{-1} , including NGC 2683, NGC 2992, NGC 3735, NGC 4845, and NGC 5792. In the nucleus of NGC 2992, the spectra reveal a double-peaked structure with a total emission line width of 587 km s^{-1} for $^{12}\text{CO } J = 1 - 0$ and 620 km s^{-1} for $^{12}\text{CO } J = 2 - 1$ (see Fig. 2), primarily driven by the rotation of the disk in the nuclear region. There is an extremely active AGN at the center of NGC 2992 (Gilli et al. 2000), with multi-wavelength evidence revealing AGN-driven outflows and winds (e.g., Irwin et al. 2017; Zanchettin et al. 2023).

We fitted the CO emission lines with multiple (up to three) Gaussian components to determine the centroid velocities and calculated the integrated intensities of different CO lines for each galaxy by summing the area over the velocity range of ΔW . As $^{12}\text{CO } J = 1 - 0$ is the strongest line in most cases, its line emission velocity range is marked by the black box in Fig. 1. For the $^{13}\text{CO } J = 1 - 0$ and $^{12}\text{CO } J = 2 - 1$ lines, which are not detected, we adopt the same velocity range as $^{12}\text{CO } J = 1 - 0$. However, when these lines are detected with a S/N greater than 3σ , the velocity window is determined based on their actual line shapes and shown as the red box. Subsequently, we calculated the ratios between different CO emission lines, considering the beam dilution factor to correct for intensity variations caused by differences in the half power beam width at different frequencies, consistent with the method used in Paper I. The beam dilution factors for the $^{12}\text{CO } J = 1 - 0$, $^{13}\text{CO } J = 1 - 0$ and $^{12}\text{CO } J = 2 - 1$ lines are

$J = 2 - 1$ ratios typically ranged from 0.87 to 1.08 (median 0.92) and from 0.34 to 0.61 (median 0.42), respectively. An exception was made for the $^{12}\text{CO } J = 1 - 0$ / $^{12}\text{CO } J = 2 - 1$ ratio in NGC 4845 and NGC 5792, where the beam dilution correction factor ranged from 0.37 to 1.15 and 0.32 to 3.15, respectively, due to the exceptionally strong CO emission in both lines from the galactic nucleus.

When we estimated the optical depth ($\tau_{^{13}\text{CO}}$) and kinetic temperature (T_{K}) of the molecular gas under LTE (the local thermal equilibrium) conditions, we adopted the following assumptions. We assumed that both $^{12}\text{CO } J = 1 - 0$ and $^{13}\text{CO } J = 1 - 0$ have the same excitation temperature and filling factor, with $\tau_{^{12}\text{CO}} \gg 1$ and $\tau_{^{13}\text{CO}} \ll 1$. These assumptions were generally valid for galaxies in our sample that do not exhibit extreme conditions such as intense nuclear starbursts. With the abundance ratio of $^{12}\text{CO}/^{13}\text{CO}$ generally ranging from 60 to 90 in molecular clouds (Hollenbach & Thronson 1987), we followed Cormier et al. (2018) by adopting a value of 60. When calculating the kinetic temperature, we assumed an abundance ratio of $^{12}\text{CO}/\text{H}_2$ of 8×10^{-5} (Frerking et al. 1982). Detailed formulas for these calculations are provided in Paper I, and the results are summarized in Table 3. The calculation of uncertainties follows the method described in Paper I, employing 5000 boot-strap samples to determine the distributions of each measurement. All uncertainties are estimated statistically from the measurements.

3. Result

3.1. Radial distribution and total mass of molecular gas

In this subsection, we present the spatial distribution of the $^{12}\text{CO } J = 1 - 0$, $J = 2 - 1$, and $^{13}\text{CO } J = 1 - 0$ lines along the galactic disk, and compare the total molecular gas mass (M_{H_2}) estimated from the ^{12}CO and $^{13}\text{CO } J = 1 - 0$ lines. The radial CO line and H_2 column density profiles for each galaxy are provided in the appendix, with an example of NGC 2613 shown in Fig. 3. For almost galaxies, the line intensity decreases with radius.

Both $^{12}\text{CO } J = 1 - 0$ and $^{13}\text{CO } J = 1 - 0$ are used to measure the molecular gas column density, with the former usually stronger but optically thick. $^{13}\text{CO } J = 1 - 0$ is

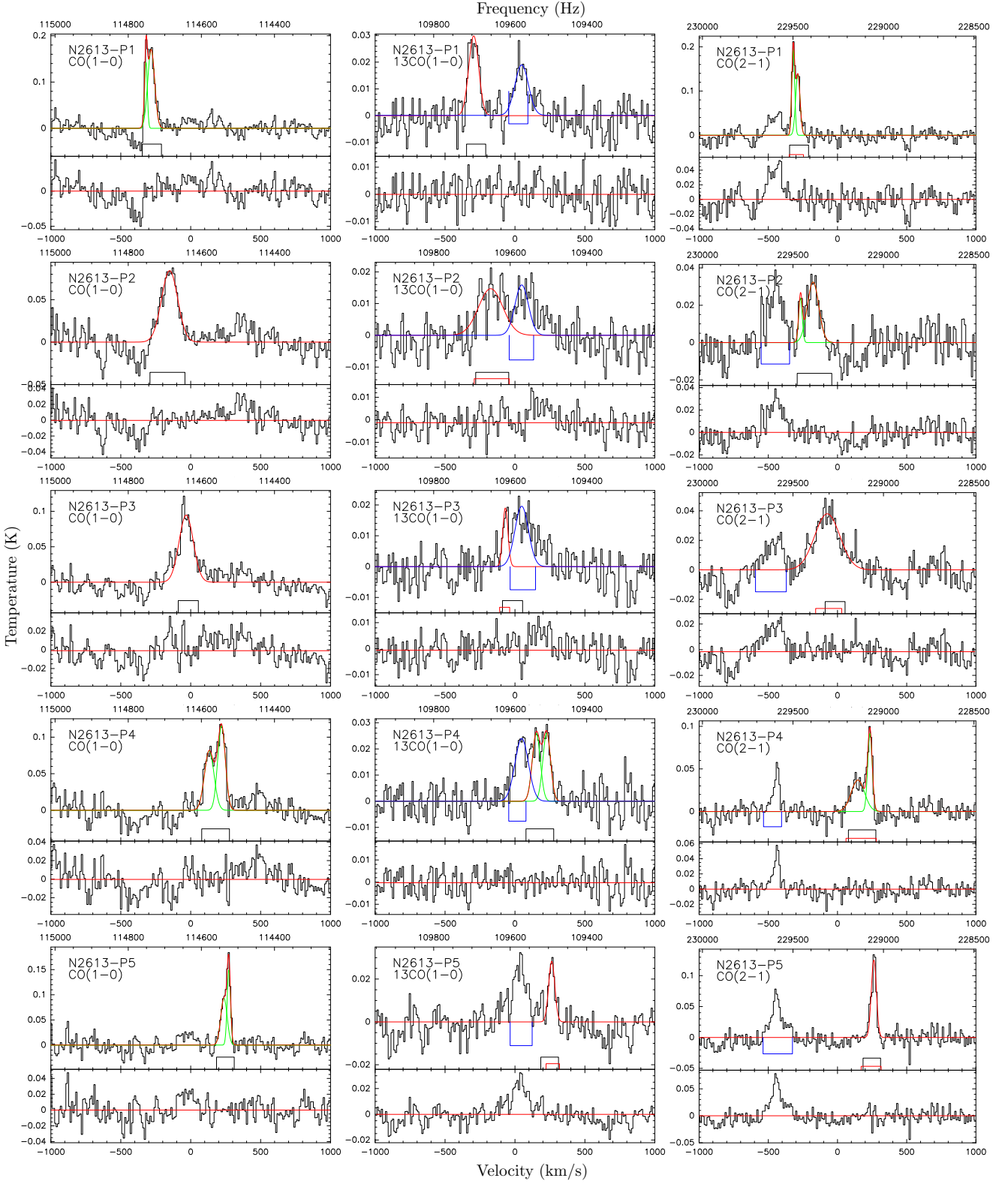


Fig. 1. $^{12}\text{CO } J = 1 - 0$ (left), $^{13}\text{CO } J = 1 - 0$ and (middle), and $^{12}\text{CO } J = 2 - 1$ (right) spectra of NGC 2613. Each row represents a different locations, as shown in Fig. 3. In the upper half of each panel, the y -axis is the main beam temperature after correcting for the main beam forward efficiency. The lower half of each panel shows the residual of the best-fit. The top x -axis indicates the frequency range for the three different molecular lines of each galaxy, set according to the zero velocity, which is defined by the galaxy's systematic velocity (Irwin et al. 2012). All spectra are binned to a velocity resolution of 10 km s^{-1} . The green curves represent the best-fit Gaussian lines, and the red line is the baseline. The blue curve represents the fitted RFI, as detailed in Sect. 2.2. The black box indicates the velocity range (ΔW) determined by the $^{12}\text{CO } J = 1 - 0$ linewidth, which is used as the fitting range. This range is also displayed on the $^{13}\text{CO } J = 1 - 0$ and $^{12}\text{CO } J = 2 - 1$ spectra to show the position of the ^{12}CO emission line. If there is a deviation, the red box highlights the adjusted velocity range used for fitting the other lines. The blue boxes mask some low-significance features which could be artificial and may slightly affect the fitting. These features are masked from the fitting and the calculation of the rms.

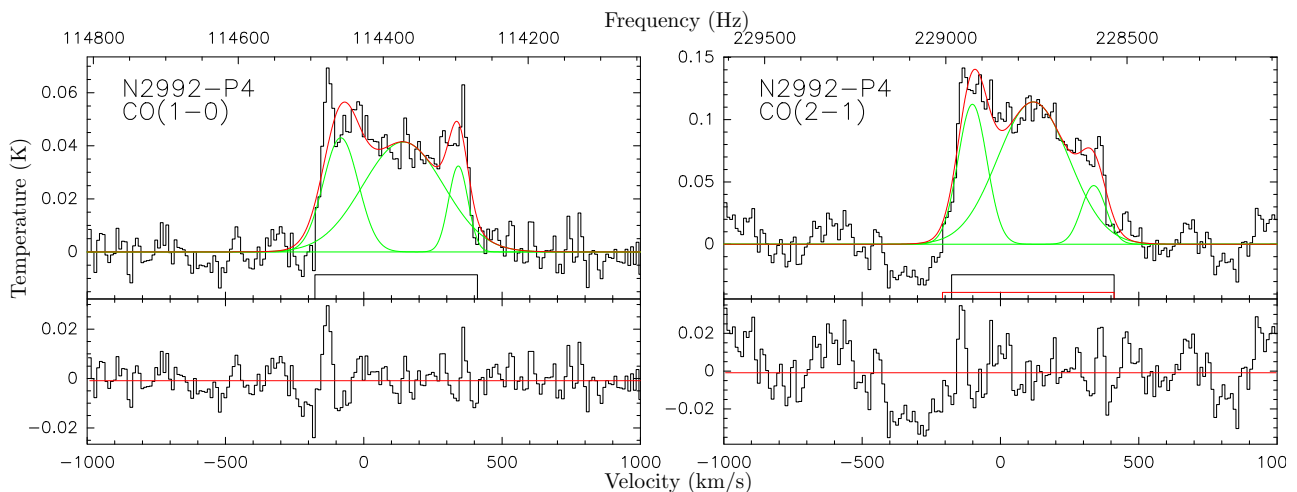


Fig. 2. The spectra of $^{12}\text{CO } J = 1 - 0$ (left panel) and $^{12}\text{CO } J = 2 - 1$ (right panel) for NGC 2992 are presented in the same format as in Fig. 3.

Table 3. Observed and derived parameters of the CO lines.

Galaxy	d (kpc)	$I_{12\text{CO}10}$ (K km s $^{-1}$)	$v_{12\text{CO}10}$ (km s $^{-1}$)	$I_{13\text{CO}10}$ (K km s $^{-1}$)	$v_{13\text{CO}10}$ (km s $^{-1}$)	$I_{12\text{CO}21}$ (K km s $^{-1}$)	$v_{12\text{CO}21}$ (km s $^{-1}$)	$\frac{^{12}\text{CO}10}{^{13}\text{CO}10}$	$\frac{^{12}\text{CO}21}{^{12}\text{CO}10}$	$\tau(^{13}\text{CO})$	T_K
(1)	(2)	(3)	(4)	(5)	(6)	(7)	(8)	(9)	(10)	(11)	(12)
N2613-1	-7.5	14.3 ± 0.6	$-291.5^{+2.6}_{-2.4}$	2.5 ± 0.3	-294.8 ± 4.6	10.7 ± 0.5	$-302.6^{+3.9}_{-3.0}$	$5.2^{+0.3}_{-0.5}$	0.28 ± 0.01	0.2	
N2613-2	-2.5	11.9 ± 0.8	-150.6 ± 4.5	< 0.8	-173.4 ± 8.6	4.0 ± 0.6	$-193.4^{+7.6}_{-6.4}$	—	$0.15^{+0.01}_{-0.03}$		
N2613-3	0.0	9.9 ± 0.6	-32.0 ± 3.7	< 0.6	-68.6 ± 5.0	5.9 ± 0.5	-73.9 ± 8.2	—	$0.24^{+0.01}_{-0.02}$		
...				

Notes. Listed items (The full version is only available online.): (1) Galaxy labels for different observational regions, as shown in Fig. 3. The bold name indicate companion galaxies or locations off the main disk, as listed in Table 2. (2) d denotes the projected distance to the galaxy’s minor axis. (3), (5), (7) The integrated line intensities for $^{12}\text{CO } J = 1 - 0$, $^{13}\text{CO } J = 1 - 0$ and $^{12}\text{CO } J = 2 - 1$ lines, corrected for main beam and forward efficiencies. If the lines are not firmly detected, we list the 3σ upper limit, and use ‘.’ in the velocity column and other parameter calculations. (4), (6), (8) The centroid velocities are derived from the intensity-weighted average velocity of the Gaussian components. (9), (10) The intensity line ratios of $^{12}\text{CO } J = 1 - 0$ to $^{13}\text{CO } J = 1 - 0$ and $^{12}\text{CO } J = 2 - 1$ to $^{12}\text{CO } J = 1 - 0$ are corrected for beam dilution as discussed in Sect. 2.2. (11), (12) $\tau(^{13}\text{CO})$ and T_K represent the optical depth and kinetic temperature, respectively, under local thermodynamic equilibrium (LTE). The uncertainties only account for the statistical errors from the measurements.

typically regarded as optically thin and a reliable tracer of molecular hydrogen in regions with a higher proportion of dense gas. However, in the normal galactic disk, it is less sensitive to the diffuse phase of molecular gas (Cormier et al. (2018)). Cormier et al. (2018) conducted a study on the spatially resolved $^{13}\text{CO}(1-0)$ -to- H_2 conversion factor in disks of nearby galaxies, finding that the average value for the entire galaxy sample is $X_{^{13}\text{CO}(1-0)} = 1.0 \times 10^{21} \text{ cm}^{-2}/(\text{K km s}^{-1})$, with an uncertainty of approximately a factor of 2 due to calibration uncertainties, including variations in CO line ratios, dust properties, and stellar populations.

We employ an X factor of $X_{^{12}\text{CO}(1-0)} = 2 \times 10^{20} \text{ cm}^{-2}/(\text{K km s}^{-1})$ for $^{12}\text{CO } J = 1 - 0$ to calculate the molecular gas column density N_{H_2} . The X factor generally varies with several parameters of a molecular cloud, such as temperature, optical depth, column density, and metallicity. In general, there is good agreement on the estimated X factors through various inde-

pendent predictions and observations, such as estimates from the dynamics of molecular clouds (e.g., Solomon et al. 1987), isotopologues (e.g., Goldsmith et al. 2008), extinction (e.g., Frerking et al. 1982), dust emission (e.g., Dame et al. 2001), and gamma-ray emission (e.g., Strong & Mattox 1996). These methods yield an X factor of approximately $X_{^{12}\text{CO}(1-0)} \approx (1 \sim 4) \times 10^{20} \text{ cm}^{-2}/(\text{K km s}^{-1})$ (Shetty et al. 2011). No matter these studies focus on larger masses, higher resolution scales, or nearby normal star-forming galaxies, the conclusions are generally consistent with those in the Milky Way, with deviations around 40 percent in extragalactic environments (e.g., Rosolowsky & Leroy 2006; Bolatto et al. 2013). Previous studies have generally concluded that galaxy centers exhibit lower X factors (e.g., Sandstrom et al. 2013; Bolatto et al. 2013), likely due to higher temperatures, increased velocity dispersion, and elevated metallicity (e.g., Henry & Worthey 1999). Those effects may become even more pronounced in galaxies with AGN activity at their centers (e.g., Papadopoulos & Seaquist 1999; Yao et al. 2003). To maintain consis-

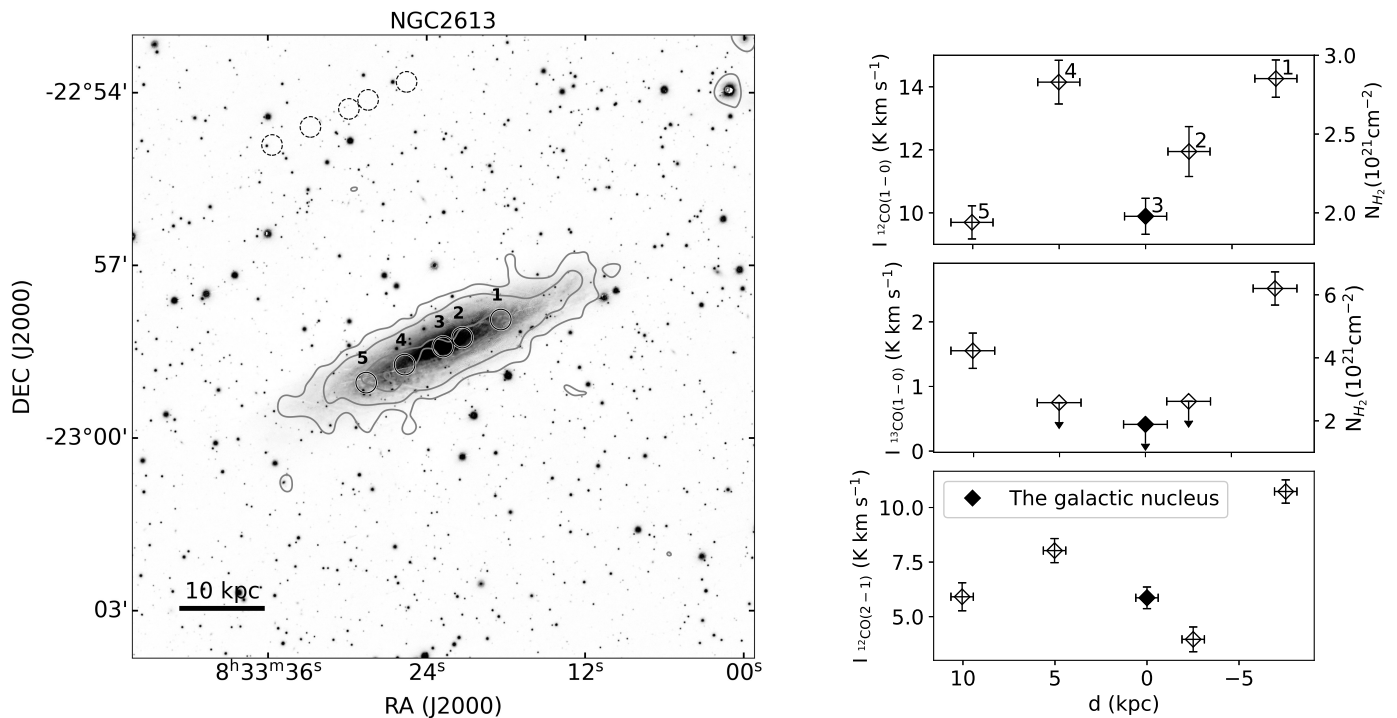


Fig. 3. *Left panel:* The *Pan – STARSS* g -band image displays an 11 arcmin \times 11 arcmin area centered on NGC 2613. The solid circles indicate the location of IRAM 30m beams with a $\approx 21.4''$ diameter for the $^{12}\text{CO } J = 1 - 0$ spectral band. The dashed circles represent the background location for the PSW observations. The overlay contours are from a convolved $22 \mu\text{m}$ image from the WISE archive. For most galaxies, contour levels include 3σ , 10σ , and 50σ , with additional levels at 100σ and 150σ for those with more pronounced flux peaks, where 3σ corresponds to a median flux of 0.01 mJy. UGC 10288 is an exception, where the contour levels are 3σ and 10σ . *Right panel:* The right panel displays the integrated intensities of the $^{12}\text{CO } J = 1 - 0$ (top row), $^{13}\text{CO } J = 1 - 0$ (middle row) and $^{12}\text{CO } J = 2 - 1$ (bottom row) lines along the galaxy disk, corresponding to the numbered positions in the left panel. The filled diamond indicates the galaxy nucleus. The x-axis represents the projected distance to the minor axis as listed in Table 3. The right y-axes of the top two panels show the molecular gas column density N_{H_2} , derived from the corresponding line.

tency with the methodology used for deriving molecular gas masses from $^{13}\text{CO } J = 1 - 0$, we adopt the same X factor value for both the centers and disks. In our subsequent discussions, we will compare molecular gas mass estimates based on both $^{12}\text{CO } J = 1 - 0$ and $^{13}\text{CO } J = 1 - 0$.

We measure the CO line flux at a few isolated positions along the disk of each galaxy. In order to estimate the total molecular gas mass of the galaxy, we need to apply a reasonable scaling factor between our directly measured CO line flux and the same line flux integrated over the whole galaxy. Here we simply assume the CO line flux has a constant ratio to the IR flux, which traces the dust-obscured emissions mainly from SF regions (e.g. Kennicutt 1998; Kennicutt & Evans 2012; Leroy et al. 2008). We adopt the $22 \mu\text{m}$ flux from the Wide-field Infrared Survey Explorer (WISE) survey, as it is uniformly available for all our sample galaxies (Vargas et al. 2019) and is little impacted by the extinction effect (however, see Li et al. 2016a for the potential extinction effect for edge-on galaxies. In the study by Vargas et al. (2018), edge-on galaxies were found to exhibit an average reduction in $25 \mu\text{m}$ flux by a factor of 1.36 due to extinction when compared to face-on galaxies. This effect has not been accounted for in our analysis.). We reprocess the WISE $22 \mu\text{m}$ images by subtracting a local background and convolving them to a resolution of $21''$ (the IRAM 30m main beam size at $^{12}\text{CO } J = 1 - 0$) using convolution kernels provided by Aniano et al. (2011). We calculate the

total $22 \mu\text{m}$ flux within the contour defined at a level of three times the background standard deviation (3σ), which is often comparable in radial extension to the regions covered by our CO line observations. The scaling factor used to correct for the directly measured CO line flux (f_{IR} ; see Table 4) is defined as the ratio between the $22 \mu\text{m}$ fluxes measured within the IRAM 30m beams (characterized with isolated circular regions) and the 3σ IR contour of the galaxy. Here we exclude the nuclear region of the galaxy, as it sometimes shows unusually strong IR emissions from the active galactic nuclei (AGN) that do not correlate to the CO line emissions. The molecular gas mass measured from the beam covering this nuclear region is directly added to the total mass of the galaxy.

The total molecular gas mass, derived from the corrected molecular gas mass in the disk ($f_{\text{IR}} \times M_{\text{H}_2, \text{disk}}^{\text{O}}$) plus the original molecular gas mass from the nuclear region ($M_{\text{H}_2, \text{nucleus}}^{\text{O}}$), is summarized in Table 4. For NGC 2683, NGC 4244, and NGC 2820, we define a single elliptical region to calculate the correction factor f_{IR} , ensuring that only the IR flux from the galaxy itself is included. Specifically, for NGC 2683 and NGC 4244, the 3σ IR contours are fragmented into multiple discrete regions across their disks. For NGC 2820, the elliptical region is used to distinguish the galaxy's IR flux from that of its companion galaxies. For consistency, we recalculated the total molecular gas mass of

NGC 4594 from Paper I using the same method, and found negligible difference.

The infrared and radio emissions in an AGN core, where the $22\ \mu\text{m}$ flux is heavily influenced by AGN activity, differ from those in star formation regions, so the calculation for the nucleus is flawed. Thus, we apply a modified method to galaxies where the nucleus flux exceeds ten times the average flux of the galaxy disk, including NGC 2992, NGC 3448, NGC 4845, and NGC 5792. For NGC 2992, NGC 3448, and NGC 4845, the total masses of molecular gas are obtained by summing the original molecular gas mass from both the disk and nucleus. However, given the compactness of NGC 5792 and the limitations of IR resolution, we use the $\text{H}\alpha$ image from Vargas et al. (2019) to derive the scaling factor. The higher resolution $\text{H}\alpha$ image helps us to separate the inner ring or other stellar/gaseous structures from the galactic nucleus. Similarly, we then calculate the scaling factor as the ratio of the total $\text{H}\alpha$ flux within the IRAM 30m beam or within the $22\ \mu\text{m}$ 3σ contour, both excluding the flux from the nuclear region. This approach ensures consistency with the method applied to other galaxies in terms of area definition, while the scaling factor itself is based entirely on the $\text{H}\alpha$ flux.

For comparison, we also derive the total molecular gas mass from the $^{13}\text{CO}\ J = 1 - 0$ emission using the same method and scaling factor as for $^{12}\text{CO}\ J = 1 - 0$. The results are listed in Table 4. We compare the two masses in Fig. 4, and find that for most of the galaxies these two masses show a tight linear correlation, but the molecular gas mass derived from $^{13}\text{CO}\ J = 1 - 0$ may be systematically smaller, with a median value of $M_{\text{H}_2,^{13}\text{CO}}/M_{\text{H}_2,^{12}\text{CO}}$ ratio of 0.70 ± 0.08 and a fitted slope of 0.77 ± 0.03 in log space. The discrepancies between the molecular gas mass derived from $^{12}\text{CO}\ J = 1 - 0$ emission and those derived from $^{13}\text{CO}\ J = 1 - 0$ emission are most likely due to the differences in the X factor dependences on galaxies or environments as discussed above in this section, which is not considered in our calculations. For the high-mass end, there may be an overestimation of the $X_{^{12}\text{CO}(1-0)}$ factor, as evidenced by $M_{\text{H}_2,^{12}\text{CO}}$ being greater than $M_{\text{H}_2,^{13}\text{CO}}$ in the galaxy disk, and in the nucleus regions where $M_{\text{H}_2,^{12}\text{CO,nucleus}}$ also exceeds $M_{\text{H}_2,^{13}\text{CO,nucleus}}$. Moreover, the slightly higher critical density for excitation of $^{13}\text{CO}\ J = 1 - 0$ emission ($\sim 600\ \text{cm}^{-3}$; Jiménez-Donaire et al. 2017; Cormier et al. 2018) compared to $^{12}\text{CO}\ J = 1 - 0$ makes it weaker or undetectable in more diffuse regime, particularly across most galactic disks in our sample. Compared with resolved observations from ALMA (Atacama Large Millimetre/submillimetre Array), such as NGC 2992 (Zanchettin et al. 2023) and NGC 4594 (Sutter & Fadda 2022), the total molecular gas mass derived using the same X factor shows no significant variation. In the subsequent discussions, we will only adopt the molecular gas mass derived from the $^{12}\text{CO}\ J = 1 - 0$ line.

3.2. CO line ratios and physical conditions of molecular gas

In this section, we present the measured $^{12}\text{CO}/^{13}\text{CO}\ J = 1 - 0$ and $^{12}\text{CO}\ J = 2 - 1/J = 1 - 0$ line ratios (Fig. 5), and derive some physical parameters based on them.

The $^{12}\text{CO}/^{13}\text{CO}\ J = 1 - 0$ ratio can be affected by both the optical depth and the isotopic abundance of the molecular cloud. In regions with active SF, the ^{12}CO emission is enhanced in warm, diffuse clumps due to a signif-

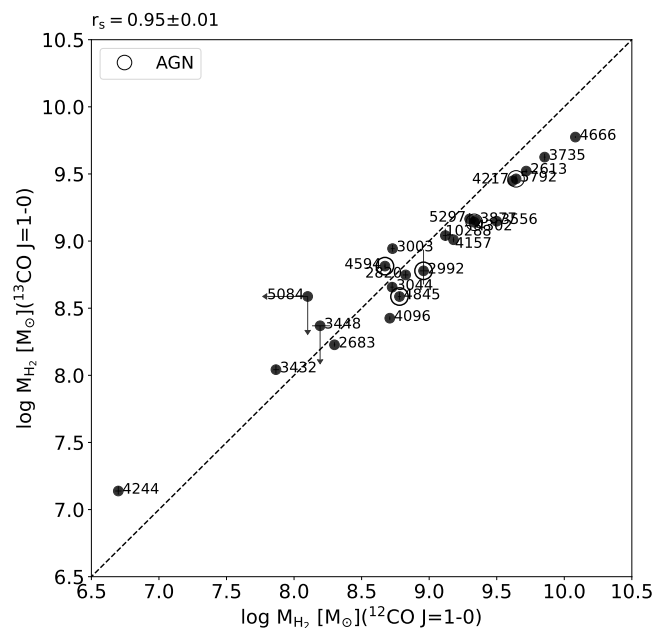


Fig. 4. Comparison of the total molecular gas mass derived from the $^{12}\text{CO}\ J = 1 - 0$ and $^{13}\text{CO}\ J = 1 - 0$ lines for 23 galaxies in our sample. The dashed line represents the 1:1 ratio. Galaxies hosting ERB (extremely radio bright) AGNs, which may significantly influence the measurements of radio flux density, are marked with a thick black circle, while those with RB (radio bright) AGNs, less likely to strongly affect the radio flux measurements, are marked with a thin black circle. These AGNs are labeled as 'ERB' and 'RB,' respectively, in the last column of Table 1 in Li et al. (2016a).

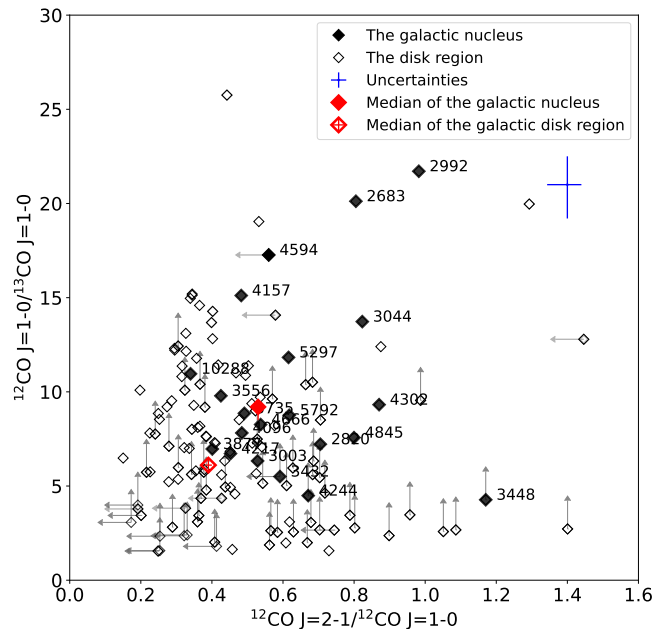


Fig. 5. A comparison of the $^{12}\text{CO}/^{13}\text{CO}\ J = 1 - 0$ and $^{12}\text{CO}\ J = 2 - 1/J = 1 - 0$ line ratios for 23 galaxies in our sample. The disk regions and galactic nuclei are represented with open and filled symbols, respectively. The blue lines show the mean error for points without upper or lower limits. The red symbols represent the median value for the sample.

Table 4. Molecular gas mass of the sample galaxies.

Name	f_{IR}	$M_{\text{H}_2, \text{disk}}^{\text{O}}$ ($\times 10^8 M_{\odot}$)	$M_{\text{H}_2, \text{disk}}$ ($\times 10^8 M_{\odot}$)	$M_{\text{H}_2, \text{nucleus}}^{\text{O}}$ ($\times 10^8 M_{\odot}$)	M_{H_2} ($\times 10^8 M_{\odot}$)	$M_{\text{H}_2, ^{13}\text{CO}}$ ($\times 10^8 M_{\odot}$)	$\Sigma_{\text{M}_{\text{H}_2}}$ ($M_{\odot} \text{ pc}^{-2}$)
(1)	(2)	(3)	(4)	(5)	(6)	(7)	(8)
NGC2613	6.79	$7.47^{+0.88}_{-0.84}$	$50.7^{+6.0}_{-5.7}$	1.48 ± 0.33	52.3 ± 5.6	$33.2^{+9.4}_{-8.7}$	$5.86^{+0.67}_{-0.56}$
NGC2683	5.53	$0.31^{+0.03}_{-0.02}$	$1.73^{+0.15}_{-0.13}$	$0.26^{+0.03}_{-0.04}$	$1.99^{+0.15}_{-0.13}$	$1.69^{+0.36}_{-0.32}$	$2.87^{+0.22}_{-0.20}$
NGC2820	4.09	$1.21^{+0.31}_{-0.32}$	$4.95^{+1.28}_{-1.31}$	$1.73^{+0.27}_{-0.28}$	$6.70^{+1.14}_{-1.09}$	$5.60^{+1.79}_{-1.47}$	$4.53^{+0.81}_{-0.68}$
NGC2992	–	$1.47^{+0.88}_{-0.53}$	–	$7.55^{+1.11}_{-1.06}$	$9.08^{+1.32}_{-1.36}$ *	$6.00^{+3.02}_{-1.88}$ *	$7.33^{+0.93}_{-1.23}$
NGC3003	4.88	$0.90^{+0.19}_{-0.16}$	$4.42^{+0.94}_{-0.78}$	$0.94^{+0.29}_{-0.33}$	$5.36^{+1.08}_{-0.88}$	$8.79^{+2.89}_{-2.36}$	$0.89^{+0.18}_{-0.14}$
NGC3044	3.60	$1.13^{+0.14}_{-0.16}$	$4.07^{+0.52}_{-0.59}$	$1.26^{+0.18}_{-0.20}$	$5.32^{+0.55}_{-0.61}$	$4.54^{+1.42}_{-1.02}$	$2.06^{+0.21}_{-0.25}$
NGC3432	4.42	$0.15^{+0.04}_{-0.03}$	$0.67^{+0.16}_{-0.15}$	0.06 ± 0.03	$0.73^{+0.17}_{-0.15}$	$1.10^{+0.42}_{-0.32}$	$0.95^{+0.22}_{-0.19}$
NGC3448	–	$0.83^{+0.26}_{-0.21}$	–	$0.71^{+0.32}_{-0.36}$	$1.56^{+0.46}_{-0.44}$ *	< 2.3 *	$1.28^{+0.39}_{-0.36}$
NGC3556	4.71	6.31 ± 0.15	29.7 ± 0.7	1.90 ± 0.08	$31.6^{+0.7}_{-0.6}$	14.1 ± 1.7	$6.48^{+0.13}_{-0.12}$
NGC3735	3.34	$16.9^{+1.3}_{-1.2}$	$56.6^{+4.3}_{-3.9}$	$14.9^{+1.1}_{-1.3}$	$71.5^{+3.9}_{-4.0}$	$42.2^{+8.9}_{-8.1}$	$7.67^{+0.39}_{-0.41}$
NGC3877	7.54	$2.66^{+0.13}_{-0.15}$	$20.0^{+1.0}_{-1.1}$	$2.07^{+0.16}_{-0.14}$	$22.1^{+1.0}_{-1.1}$	$14.3^{+2.4}_{-2.6}$	$8.29^{+0.37}_{-0.44}$
NGC4096	7.60	0.61 ± 0.04	$4.60^{+0.28}_{-0.31}$	0.51 ± 0.04	$5.11^{+0.31}_{-0.32}$	$2.66^{+0.61}_{-0.60}$	$4.70^{+0.27}_{-0.28}$
NGC4157	3.80	$3.65^{+0.21}_{-0.22}$	13.9 ± 0.8	1.27 ± 0.15	15.1 ± 0.8	10.2 ± 1.7	$6.95^{+0.28}_{-0.40}$
NGC4217	3.40	10.8 ± 0.2	36.8 ± 0.8	$4.59^{+0.23}_{-0.25}$	41.4 ± 0.8	$28.1^{+2.2}_{-2.4}$	$9.66^{+0.17}_{-0.19}$
NGC4244	3.53	0.013 ± 0.003	0.05 ± 0.01	0.003 ± 0.001	0.05 ± 0.01	$0.14^{+0.04}_{-0.03}$	0.029 ± 0.006
NGC4302	4.85	$3.92^{+0.17}_{-0.21}$	$19.0^{+0.8}_{-1.0}$	2.55 ± 0.20	21.6 ± 0.9	13.8 ± 1.8	$5.90^{+0.22}_{-0.28}$
NGC4594	4.66	$1.00^{+0.08}_{-0.09}$	$4.66^{+0.37}_{-0.42}$	0.05 ± 0.01	$4.71^{+0.35}_{-0.39}$	$6.51^{+1.30}_{-1.12}$	$1.23^{+0.08}_{-0.10}$
NGC4666	5.83	18.2 ± 0.4	$105.9^{+2.2}_{-2.1}$	$14.9^{+0.4}_{-0.5}$	$120.8^{+2.2}_{-2.1}$	$59.5^{+5.7}_{-5.0}$	14.8 ± 0.3
NGC4845	–	$1.13^{+0.15}_{-0.16}$	–	$4.90^{+0.11}_{-0.15}$	6.03 ± 0.18 *	$3.86^{+0.57}_{-0.56}$ *	7.13 ± 0.22
NGC5084	–	–	–	–	< 1.3	< 3.9	–
NGC5297	3.38	$5.24^{+0.52}_{-0.54}$	17.7 ± 1.8	$2.17^{+0.42}_{-0.45}$	$19.9^{+1.7}_{-1.8}$	$14.6^{+4.7}_{-4.4}$	$3.80^{+0.28}_{-0.33}$
NGC5792	2.83^{**}	$11.3^{+0.8}_{-0.9}$	$32.1^{+2.3}_{-2.6}$	11.8 ± 0.7	$44.0^{+2.5}_{-2.7}$ **	$29.1^{+5.5}_{-4.9}$ **	$9.97^{+0.52}_{-0.58}$
UGC10288	2.46	$4.55^{+0.39}_{-0.53}$	$11.2^{+1.0}_{-1.3}$	$1.96^{+0.42}_{-0.47}$	$13.2^{+1.0}_{-1.1}$	$11.0^{+3.4}_{-2.4}$	$3.69^{+0.32}_{-0.37}$

Notes. Galaxies parameters. (1) Galaxy name. (2) f_{IR} is the scaling factor derived from the $22 \mu\text{m}$ flux within 3σ contour divided by the $22 \mu\text{m}$ flux within FWHM of $^{12}\text{CO } J = 1 - 0$ observation, both subtract the flux within nuclear region. Mark with “**” uses scaling factor derived from $\text{H}\alpha$ images (See Sect. 3.1 for details.). (3) $M_{\text{H}_2, \text{disk}}^{\text{O}}$ is the original molecular gas mass from all the IRAM observed positions except nuclear region. (4) $M_{\text{H}_2, \text{disk}}$ is the corrected molecular gas mass, calculated by multiplying $M_{\text{H}_2, \text{disk}}^{\text{O}}$ by f_{IR} . (5) $M_{\text{H}_2, \text{nucleus}}^{\text{O}}$ is the original molecular mass from nuclear region. Those original molecular mass estimate from $^{12}\text{CO } J = 1 - 0$ and assume the filling factor f within the beam as $\propto f^{-1}$. (6) M_{H_2} is the total molecular gas mass we use in the Sect. 4 and derived by summing the $M_{\text{H}_2, \text{disk}}$ and $M_{\text{H}_2, \text{nucleus}}^{\text{O}}$, except for the value marked with “*”. Mark with “*” is just obtained from original data of $M_{\text{H}_2, \text{nucleus}}^{\text{O}}$ and $M_{\text{H}_2, \text{disk}}^{\text{O}}$. (7) $M_{\text{H}_2, ^{13}\text{CO}}$ is the total molecular gas mass derived from $^{13}\text{CO } J = 1 - 0$ emission with the same method and f_{IR} as for $^{12}\text{CO } J = 1 - 0$. (8) $\Sigma_{\text{M}_{\text{H}_2}}$ is the total molecular gas surface density calculated using the $22 \mu\text{m}$ diameter. The uncertainties are limited to the statistical errors derived from the measurements.

icant decrease in the optical depth of the ^{12}CO -rich envelopes, which allows more ^{12}CO photons to escape. In colder molecular clouds, the abundance of ^{13}CO increases primarily through isotope exchange reactions. Additionally, ^{13}C can be produced during the CNO cycle in intermediate-mass stars’ envelopes (Truran 1977). These combined factors in environments with intense SF can lead to an elevated $^{12}\text{CO}/^{13}\text{CO } J = 1 - 0$ line ratio (e.g., Tan et al. 2011; Jiménez-Donaire et al. 2017; Cormier et al. 2018). In our sample, the $^{12}\text{CO}/^{13}\text{CO } J = 1 - 0$ ratio in the galactic nucleus is slightly higher than that in the galactic disk, and also slightly higher than the ratio observed in the Milky Way’s center (Solomon et al. 1979). This may be due to the influence of a few galaxies with particularly intense star formation activity in their nuclear regions. The median value

of the $^{12}\text{CO}/^{13}\text{CO } J = 1 - 0$ ratio for the galactic nucleus is $8.6^{+0.4}_{-0.9}$ with a typical range of 6-23. In contrast, the median value for the galactic disk is 6.1 ± 0.4 , with a typical range of 1-19. Both single-pointing (e.g., Aalto et al. 1995; Crocker et al. 2012) and spatially resolved observations of nearby galaxies (e.g., Paglione et al. 2001; Cao et al. 2017, 2023) show a clear variation of the $^{12}\text{CO}/^{13}\text{CO } J = 1 - 0$ ratio either between different galaxies or across individual galaxies. For normal late-type galaxies, the ratio typically varies from 5 to 15 (e.g., Meier & Turner 2004; Vila-Vilario et al. 2015; Roman-Duval et al. 2016), consistent with the measurements of our sample.

The $^{12}\text{CO } J = 2 - 1/J = 1 - 0$ ratio is primarily determined by the temperature and optical depth. It reflects

the structure and heating sources of the molecular clouds. Gas with a low $^{12}\text{CO } J = 2 - 1/J = 1 - 0$ ratio < 0.7 typically originates from the extended low-density envelopes of molecular clumps, while the high ratio in the range of 0.7-1 is also primarily influenced by optical depth (Hasegawa 1997) and tends to arise from highly concentrated molecular clumps characterized by steep density gradients and thin CO-emitting envelopes (e.g., Peñaloza et al. 2017). For very high $^{12}\text{CO } J = 2 - 1/J = 1 - 0$ ratios (> 1), the local environment has a significant influence, such as UV photons from young stars, shock waves from supernova explosions (Hasegawa 1997), or through effective heating mechanisms in extreme starburst environments (Papadopoulos et al. 2012), including factors like supersonic turbulence of the molecular clouds, cosmic ray ionization rates, and the interstellar radiation field (e.g., Peñaloza et al. 2018).

As shown in Fig. 5, the median value of the $^{12}\text{CO } J = 2 - 1/J = 1 - 0$ line ratio for the galactic nucleus is $0.53^{+0.04}_{-0.02}$, with a typical range of 0.5-1.4. The median value of this ratio in the galactic disk is 0.39 ± 0.01 with a range of 0.2-1.5. These ranges are in general comparable to measurements of other nearby galaxies (e.g., Leroy et al. 2022). Although the galactic nucleus is often expected to have a higher $^{12}\text{CO } J = 2 - 1/J = 1 - 0$ than the galactic disks (e.g., Leroy et al. 2009; den Brok et al. 2021; Yajima et al. 2021), this difference is not very significant for our sample, except for a few extreme cases. This indicates the low SF activity of most of our sample galaxies.

Under LTE conditions and some assumptions in Sect. 2.2, the distributions of $\tau_{13\text{CO}}$ and T_K are presented in Fig. 6. The equations used are the same as in Paper I and are given by:

$$\tau(^{13}\text{CO}) = -\ln\left[1 - \frac{I_{13\text{CO } (J=1-0)}}{I_{12\text{CO } (J=1-0)}}\right], \quad (1)$$

where the $I_{12\text{CO}}$ and $I_{13\text{CO}}$ are the integrated intensity of emission lines, and

$$\frac{N_{\text{H}_2}}{\text{cm}^{-2}} = 2.25 \times 10^{20} \left[\frac{\tau_{13\text{CO}}}{1 - e^{-\tau_{13\text{CO}}}} \right] \frac{I_{13\text{CO } J=1-0}}{1 - e^{-5.29/T_{\text{ex}}}}, \quad (2)$$

where the excitation temperature (T_{ex}), under LTE, can be approximated as the kinetic temperature (T_K). The $\tau_{13\text{CO}}$ in the nuclear regions of our sample galaxies is typically < 0.25 and has a median value of 0.09 ± 0.01 . This value is generally higher than the $\tau_{13\text{CO}}$ of nuclear starburst galaxies such as M82 (e.g., $\tau_{13\text{CO}} \sim 0.07$; Tan et al. 2011). The median value of the T_K in the nuclear region is $40.9^{+8.9}_{-2.1}$ K, with a typical range of 3-256. In a few galaxies with nuclear activities (e.g., NGC 2992 and NGC 3448), this value can be as high as ~ 100 K. In the nuclear region of these galaxies, the $^{12}\text{CO } J = 2 - 1/J = 1 - 0$ ratio is often $\gtrsim 1$, further suggesting the possibility additional heating from the AGN.

4. Discussion

In this section, we will compare our measured molecular gas properties and the atomic gas properties collected from archive to other galaxy properties, in order to understand the role of cold gas in galaxy evolution. In the follow-up correlation analysis, we will use Spearman's rank order coefficient (r_s ; by definition $-1 < r_s < 1$) to describe the tightness of the correlation. We consider a tight correlation

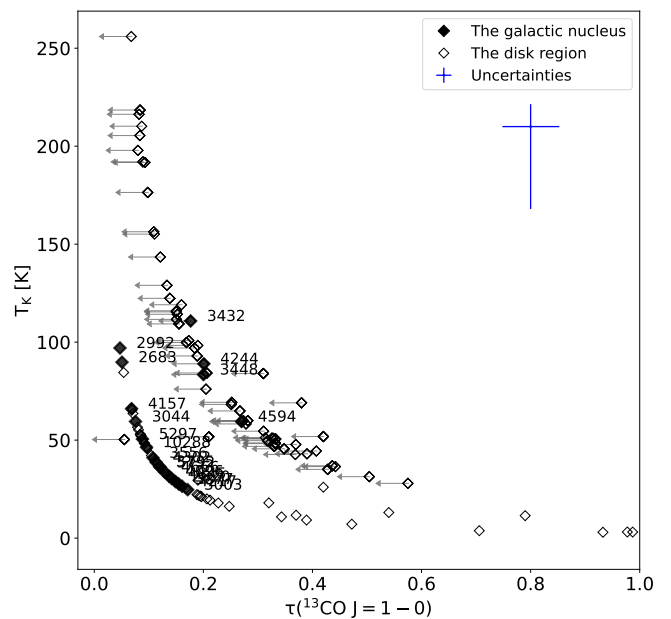


Fig. 6. The kinetic temperature (T_K) shows as a function of the optical depth of ^{13}CO ($\tau_{13\text{CO}}$), both derived from the nuclear and disk regions of the molecular gas under the assumption of LTE. The blue lines indicate mean error.

with $|r_s| > 0.6$, a weak correlation with $0.6 > |r_s| > 0.3$, and no correlation with $|r_s| < 0.3$ (e.g., Li & Wang 2013a,b). Since there is no firm detection of CO $J = 1 - 0$ in NGC 5084, this galaxy is excluded from subsequent analyses and only shows in Fig. 7.

4.1. Molecular to atomic gas mass ratio

4.1.1. Molecular and atomic gas content of the sample galaxies

There are many HI surveys of nearby galaxies reaching different detection limits and angular resolutions. For example, the THINGS survey conducted with the VLA reaches a typical HI column density detection limit of $N_{\text{HI}} \sim 10^{19} \text{ cm}^{-2}$ and an angular resolution of $30''$ (e.g., Walter et al. 2008). The HALOGAS survey conducted with the Westerbork Synthesis Radio Telescope (WSRT), typically with ~ 17 times the exposure time of THINGS, reaches a detection limit of $N_{\text{HI}} \sim 10^{19} \text{ cm}^{-2}$ and an angular resolution of $20'' - 30''$ (e.g., Heald et al. 2011). The FEASTS survey conducted with the single-dish Five-hundred-meter Aperture Spherical Telescope (FAST), without missing flux, reaches a typical detection limit of $N_{\text{HI}} \sim 10^{17.7} \text{ cm}^{-2}$ and an angular resolution of $3.2'$ (e.g., Wang et al. 2023, 2024). We consider that the contribution from low column density HI is not significant for our analysis, as the primary focus is on higher column densities that dominate the gas content in galaxies.

In this paper, since we only need the total HI gas mass within the galactic disk, we directly collect the atomic gas mass (M_{HI}) of our sample galaxies from different literatures, as summarized in Table 1. M_{HI} of 14 galaxies is obtained from the CHANG-ES VLA C-configuration HI observations presented in Zheng et al. (2022). For the other galaxies, we typically only obtain the HI flux measured with different

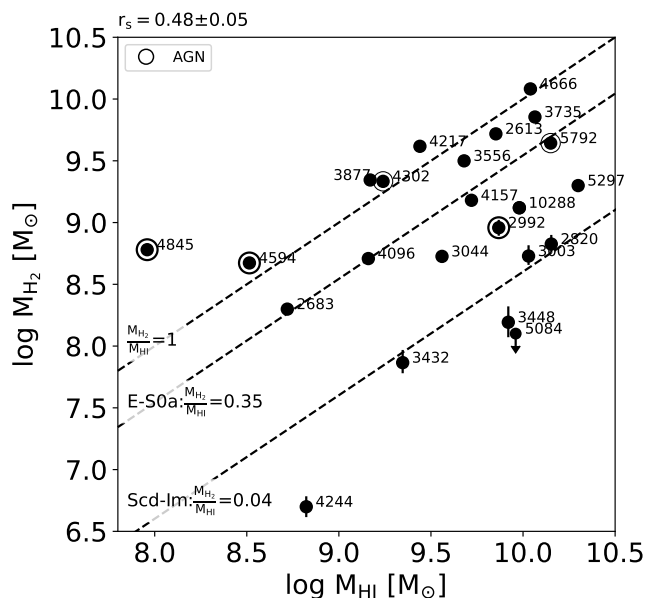


Fig. 7. M_{H_2} vs. M_{HI} . The dotted line represents the $M_{\text{H}_2}/M_{\text{HI}}$ ratio, where the median value of 0.35 and 0.04 are corresponding to different galaxy types, as obtained from Lisenfeld et al. (2011). The circle symbols represent the AGN, as shown in Fig. 4.

telescopes (Table 1), and convert them to M_{HI} using the following relation:

$$M_{\text{HI}}/M_{\odot} = 2.356 \times 10^5 S_{\text{HI}} d^2, \quad (3)$$

where S_{HI} is the integrated HI line flux in unit of Jy km s^{-1} , d is the distance to the galaxy in unit of Mpc (taken from Vargas et al. 2019). The derived M_{HI} is also summarized in Table 1.

The mass fraction of molecular and atomic gas and the transformation between them are crucial in the study of galaxy formation and evolution. Previous works (e.g., Young & Knezek 1989; Saintonge et al. 2011; Catinella et al. 2018; Lisenfeld et al. 2019) suggest a weak correlation between the mass of molecular and atomic gases in nearby galaxies. This weak correlation is also evident in our sample, as shown in Fig. 7 ($r_s \approx 0.49$). Despite the weak correlation, the scatter of M_{H_2} at a given M_{HI} is up to more than one order of magnitude, indicating a wide range of the molecular to atomic gas mass ratio, regardless of the non-uniformity of M_{HI} measurements from different literatures. The M_{H_2} - M_{HI} relation, or the $M_{\text{H}_2}/M_{\text{HI}}$ ratio, could potentially be affected by the AGN activity and the morphological type of the galaxies, as suggested in many previous works (e.g., Young & Knezek 1989; Casoli et al. 1998; Lisenfeld et al. 2011), or by some special cases. For example, there are two significant outliers in Fig. 7. NGC 4845, which has a very active AGN (Irwin et al. 2015), does not show a deficiency in molecular gas mass compared to other galaxies, but rather has the lowest atomic gas content in our sample. NGC 4244 is a low surface brightness galaxy and is one of the latest type galaxies in the CHANG-ES sample; the low molecular gas content may be consistent with its low stellar mass and SFR (both lowest in the sample; Li et al. 2016a). However, we do not find a significant trend showing such a dependence in Fig. 7. This is possibly because the CHANG-ES sample is selected without extreme AGN activities and all

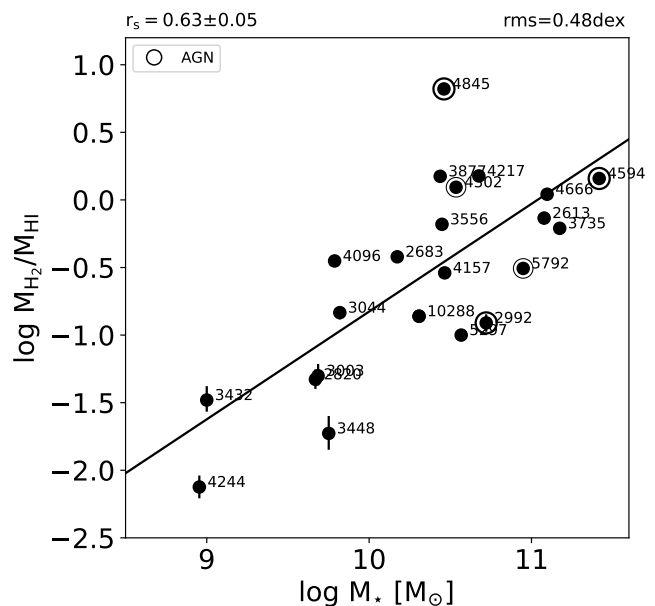


Fig. 8. The distribution of $M_{\text{H}_2}/M_{\text{HI}}$ ratio with M_* . The circle symbol of each galaxy are the same with Fig. 4.

the galaxies are spiral, in a relatively narrow morphological type range.

4.1.2. Gas mass ratio and stellar mass

In this subsection, we aim to further investigate the dependence of the molecular to atomic gas mass ratio ($M_{\text{H}_2}/M_{\text{HI}}$) on other galaxy parameters, such as the stellar mass (M_*).

Fig. 8 shows that $M_{\text{H}_2}/M_{\text{HI}}$ is strongly correlated with M_* ($r_s \approx 0.63$) in our sample, consistent with previous studies from extensive samples (e.g., Leroy et al. 2005; Saintonge et al. 2011; Lisenfeld et al. 2011; Bothwell et al. 2014; Catinella et al. 2018). We have fitted this correlation with

$$\log \frac{M_{\text{H}_2}}{M_{\text{HI}}} = (0.79 \pm 0.19) \log \left(\frac{M_*}{M_{\odot}} \right) - (8.78 \pm 2.01), \quad (4)$$

where M_* is derived from the K-band luminosity and the mass-to-light ratio, as presented in Li et al. (2016a). This relation is primarily affected by the efficiency of atomic-to-molecular gas conversion, which depends on two main factors: metallicity and pressure. The increase of M_* leads to higher metallicity and/or dust in the ISM, which shields the molecular gas from dissociation by the radiation field (e.g., Elmegreen 1993; Fu et al. 2010; Krumholz et al. 2009). Under hydrostatic equilibrium, stronger gravitational potential wells lead to higher pressures, compressing gas and increasing the column density of the gas, thereby enhancing the efficiency of atomic-to-molecular gas conversion (e.g., Elmegreen 1989, 1993; Wong & Blitz 2002; Leroy et al. 2008). The gravitational potential in galaxies can be dominated either by stars or by the self-gravity of gas, depending on the specific environment.

Galaxies with lower stellar masses, located in the lower left of Fig. 8, also appear in the lower right of Fig. 7, where their molecular gas masses are an order of magnitude lower than atomic gas mass. The primary reason is their relatively low stellar masses, which cause a shallow potential well,

lower pressure, and lower gas surface density, hindering the conversion of atomic gas into molecular gas, especially in the lowest-mass galaxy NGC 4244. Additionally, galaxies with shallow potential wells may struggle to retain their metallicity (e.g., Tremonti et al. 2004). The increase in the $M_{\text{H}_2}/M_{\text{HI}}$ ratio for NGC 4845 is mainly due to a deficiency in M_{HI} .

4.2. Star formation law

The cold atomic and molecular gas provide fuels to continue SF, with the latter directly connected to the current SF processes. The Kennicutt–Schmidt SF law describe the relationship between the surface density of the cold gas and the surface density of the SFR measured with different tracers (e.g., Kennicutt 1998; Kennicutt & Evans 2012). With spatially resolved measurement of the molecular gas distribution on the galactic disk, our sample is optimized to examine the SF law. We compare our sample to the well calibrated SF law based on similarly spatially resolved cold gas and SFR observations of nearby galaxies from Bigiel et al. (2008) in Fig. 9. We also adopt the gas depletion timescale to describe how active is the SF in the galaxy. It is defined as the timescale to consume the SF fuel at the current SFR, or the inverse of the SF efficiency: $\tau_{\text{H}_2} = M_{\text{H}_2}/\text{SFR}$.

In Fig. 9, the SF law is presented in the form of $\Sigma_{\text{SFR}} - \Sigma_{\text{H}_2}$, where we calculate Σ_{H_2} based on the total measured molecular gas mass M_{H_2} and the SF diameter of the galaxy measured with the $22\ \mu\text{m}$ data (obtained from Wiegert et al. 2015 and listed in Table 1). We directly adopt the disk-average SFR surface density Σ_{SFR} computed base on the spatially resolved $22\ \mu\text{m}$ and $\text{H}\alpha$ data (Vargas et al. 2019). In Fig. 9, we also plot the $\Sigma_{\text{SFR}} - \Sigma_{\text{H}_2}$ relationships corresponding to different gas depletion timescales. Our sample mostly falls on the best-fit relation from Bigiel et al. (2008), which corresponds to a depletion timescale of $\tau_{\text{H}_2} \sim 10^9\ \text{yr}$. This is consistent with some moderately SF galaxies (e.g., Bigiel et al. 2011; Leroy et al. 2013; Lisensfeld et al. 2019), but could be one order of magnitude larger than extreme starburst galaxies, such as luminous infrared galaxies and ultraluminous infrared galaxies, which are known to have higher SF efficiencies and shorter gas depletion timescale (e.g., Saintonge et al. 2011).

As show in Fig. 9, our sample shows a relatively large scatter compared to the usually tight correlation between Σ_{SFR} and Σ_{H_2} (e.g., Kennicutt & Evans 2012). This is mainly because of the relatively small dynamical range of both parameters in our sample, which mainly represent inactive or normal SF galaxies. Furthermore, there are a few significant outliers from the SF law, which enlarge this scatter. For example, NGC 4244 is a dwarf galaxy with small gas content and weak SF, and the IR and $\text{H}\alpha$ emissions used to calculate the SFR may be contaminated by the contributions from some old stellar components (e.g., Vargas et al. 2018, 2019). The real uncertainty of the measured Σ_{SFR} and Σ_{H_2} should be larger than those presented in Fig. 9, which include only statistical errors. NGC 2992 has an extremely active AGN and relatively small angular size. The SFR determined largely from the WISE $22\ \mu\text{m}$ data should be largely overestimated, with contributions from the strong AGN emissions. Xu et al. (2024) analyzed the stellar population in NGC 2992 and revealed that AGN outflows have suppressed SF in the nuclear region ($<1\ \text{kpc}$), but trigger increased SF activity outside the nucleus. NGC 3448

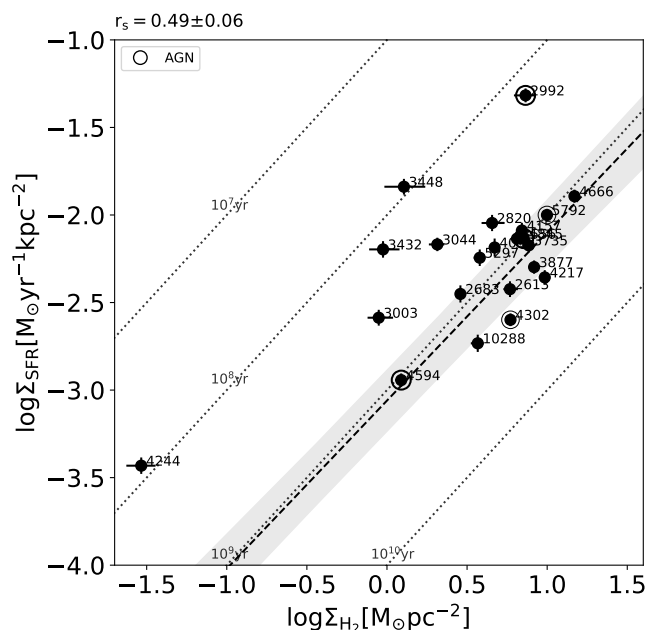


Fig. 9. The Σ_{H_2} is shown as a function of Σ_{SFR} . The AGN symbol is the same as Fig. 4. The dashed line represents the average fitting of seven galaxies in Bigiel et al. (2008), and the shaded area indicates the 1σ uncertainty of the fit. The dotted lines correspond to gas depletion times of 10^{10} , 10^9 , 10^8 and 10^7 years from bottom to the top.

also has an IR bright core, which may represent a weak AGN and cause the overestimate of the SFR, although high-resolution radio continuum observations suggest the peak of the radio emission may be off nucleus (Irwin et al. 2019). NGC 3432 has a warped disk possibly impacted by the gravitational tidal force of the dwarf companions UGC 5983 and [KMK2013] LV J1052+3639. The galaxy may be in a stage when the tidal interaction helps triggering the SF on the galactic disk (e.g., Renaud et al. 2014; Pan et al. 2018). NGC 3003 exhibits unusually large H I , $\text{H}\alpha$, and radio scales high compared to other CHANG-ES galaxies, which may be influenced by the tidal interaction (e.g., Krause et al. 2018; Lu et al. 2023).

4.3. Gas baryon budget

The fraction of baryons of a galaxy stored in different forms varies at different galaxy masses, and the gas in different phases could take a significant fraction of a galaxy’s total baryon budget (e.g., Werk et al. 2014; Li et al. 2017, 2018; Bregman et al. 2018, 2022). The baryonic Tully-Fisher relation is an empirical scaling relation between the baryonic mass M_b and the gravitation of the galaxy characterized with the rotation velocity V_{rot} (e.g., McGaugh et al. 2000). In Fig. 10, we plot our sample galaxies against the well-defined baryonic Tully-Fisher relation from McGaugh (2005), using the sum of stellar mass and total gas ($\text{H}_2 + \text{HI}$) masses, along with the rotation velocity obtained from archive (e.g., Li et al. 2016a). In follow-up papers, we will further discuss the rotation curve of our sample galaxies measured based on both our CO data (Li et al. 2019; Jiang et al. 2024) and some multi-wavelength data tracing different gas phases (e.g., Zheng et al. 2022; Li et al. 2024).

5. Summary and Conclusion

We present IRAM 30m observations of the $^{12}\text{CO } J = 1 - 0$, $^{13}\text{CO } J = 1 - 0$, and $^{12}\text{CO } J = 2 - 1$ lines along the disk of 23 nearby spiral galaxies selected from the CHANG-ES sample. We then calculate the ratios between different CO lines and derive the temperature and optical depth of the molecular gas. We further examine the dependence of the gas properties on other galaxy properties. Our main results and conclusions are summarized below:

- The $^{12}\text{CO } J = 1 - 0$, $^{13}\text{CO } J = 1 - 0$, and $^{12}\text{CO } J = 2 - 1$ lines are detected at 77%, 40%, and 73% of the observed positions along the galactic disks, and 96%, 78%, and 96% of the nuclear regions of the galaxies.

- Using the WISE 22 μm image, we rescale the molecular gas mass measured from our CO line observations of individual regions to the total molecular gas mass of each galaxy. For most galaxies, the molecular gas mass derived from $^{13}\text{CO } J = 1 - 0$ is tightly correlated with mass derived from $^{12}\text{CO } J = 1 - 0$, but systematically lower than that from $^{12}\text{CO } J = 1 - 0$, possibly caused by the uncertainties of X factor and lower detection rate of the weaker $^{13}\text{CO } J = 1 - 0$ line in the galaxy disk.

- After correcting for the beam dilution, the median values of the $^{12}\text{CO}/^{13}\text{CO } J = 1 - 0$ and $^{12}\text{CO } J = 2 - 1/J = 1 - 0$ ratios in the nucleus/disk of galaxies are $\approx 8.6/6.1$ and $0.53/0.39$, respectively. The median values of the derived kinetic temperature and optical depth under the LTE assumption in the galaxy are ≈ 41 K and 0.1, respectively. These values are all typical for non-starburst spiral galaxies.

- There is a weak correlation between the total molecular and atomic gas masses of our sample galaxies, but the molecular to atomic gas mass ratio $M_{\text{H}_2}/M_{\text{HI}}$ shows a large scatter of more than one order of magnitude. $M_{\text{H}_2}/M_{\text{HI}}$ could be affected by many factors. One of the most important ones appears to be the stellar mass of the galaxy, which shows a tight, nearly linear relation with $M_{\text{H}_2}/M_{\text{HI}}$. This correlation indicates that in galaxies with higher stellar masses, increased metallicity and stronger gravitational potential accelerate the conversion of atomic gas into molecular gas, leading to a higher $M_{\text{H}_2}/M_{\text{HI}}$ ratio. In our sample, galaxies with lower stellar masses also exhibit reduced $M_{\text{H}_2}/M_{\text{HI}}$ ratios, with the molecular gas masses in these galaxies being an order of magnitude lower than the atomic gas masses.

- Most of our sample galaxies fall close to the Kennicutt-Schmidt SF law, with a median gas depletion timescale of ~ 1 Gyr. Some galaxies show significantly shorter gas depletion timescales of ~ 0.1 Gyr, and could be affected by various measurement uncertainties, as well as some special processes prompting the SF efficiency.

- Our sample galaxies fall on the baryonic Tully-Fisher relation, except for a few most massive galaxies, which have systematically lower baryonic mass at a given rotation velocity. The missing baryonic mass of these massive spirals is largely recovered by the inclusion of the extended hot CGM. The cold gas fraction of the total baryon mass decreases with increasing gravitational potential, because the gas is consumed either in early SF or being heated to the hot phase.

ACKNOWLEDGEMENTS

The authors would like to commemorate the late Prof. Yu Gao and express their deep gratitude for his invaluable

guidance in observations and learning. The authors also acknowledge Dr. Zhi-Yu Zhang and Dr. Jian Fu for helpful discussions. J.T.L. acknowledges the financial support from the National Science Foundation of China (NSFC) through the grants 12273111, and also the science research grants from the China Manned Space Project. Q.H.T. acknowledges the support by the NSFC grant No. 12033004.

References

- Aalto, S., Booth, R. S., Black, J. H., & Johansson, L. E. B. 1995, *A&A*, 300, 369
- Aniano, G., Draine, B. T., Gordon, K. D., & Sandstrom, K. 2011, *PASP*, 123, 1218
- Behroozi, P. S., Conroy, C., & Wechsler, R. H. 2010, *ApJ*, 717, 379
- Bigiel, F., Leroy, A., Walter, F., et al. 2008, *AJ*, 136, 2846
- Bigiel, F., Leroy, A. K., Walter, F., et al. 2011, *ApJ*, 730, L13
- Bolatto, A. D., Wolfire, M., & Leroy, A. K. 2013, *ARA&A*, 51, 207
- Boselli, A., Cortese, L., Boquien, M., et al. 2014, *A&A*, 564, A66
- Bothwell, M. S., Wagg, J., Cicone, C., et al. 2014, *MNRAS*, 445, 2599
- Bregman, J. N., Anderson, M. E., Miller, M. J., et al. 2018, *ApJ*, 862, 3
- Bregman, J. N., Hodges-Kluck, E., Qu, Z., et al. 2022, *ApJ*, 928, 14
- Cao, Y., Wong, T., Bolatto, A. D., et al. 2023, *ApJS*, 268, 3
- Cao, Y., Wong, T., Xue, R., et al. 2017, *ApJ*, 847, 33
- Carter, M., Lazareff, B., Maier, D., et al. 2012, *A&A*, 538, A89
- Casoli, F., Sauty, S., Gerin, M., et al. 1998, *A&A*, 331, 451
- Catinella, B., Saintonge, A., Janowiecki, S., et al. 2018, *MNRAS*, 476, 875
- Chaves, T. A. & Irwin, J. A. 2001, *ApJ*, 557, 646
- Cicone, C., Bothwell, M., Wagg, J., et al. 2017, *A&A*, 604, A53
- Cormier, D., Bigiel, F., Jiménez-Donaire, M. J., et al. 2018, *MNRAS*, 475, 3909
- Courtois, H. M. & Tully, R. B. 2015, *MNRAS*, 447, 1531
- Crocker, A., Krips, M., Bureau, M., et al. 2012, *MNRAS*, 421, 1298
- Dame, T. M., Hartmann, D., & Thaddeus, P. 2001, *ApJ*, 547, 792
- Davis, L. E. & Seaquist, E. R. 1983, *ApJS*, 53, 269
- de Vaucouleurs, G., de Vaucouleurs, A., Corwin, Herold G., J., et al. 1991, *Third Reference Catalogue of Bright Galaxies*
- den Brok, J. S., Chatzigiannakis, D., Bigiel, F., et al. 2021, *MNRAS*, 504, 3221
- Elmegreen, B. G. 1989, *ApJ*, 338, 178
- Elmegreen, B. G. 1993, *ApJ*, 411, 170
- Evans, Neal J., I. 1999, *ARA&A*, 37, 311
- Frerking, M. A., Langer, W. D., & Wilson, R. W. 1982, *ApJ*, 262, 590
- Fu, J., Guo, Q., Kauffmann, G., & Krumholz, M. R. 2010, *MNRAS*, 409, 515
- Gilli, R., Maiolino, R., Marconi, A., et al. 2000, *A&A*, 355, 485
- Goldsmith, P. F., Heyer, M., Narayanan, G., et al. 2008, *ApJ*, 680, 428
- Hasegawa, T. 1997, in *IAU Symposium*, Vol. 170, *IAU Symposium*, ed. W. B. Latter, S. J. E. Radford, P. R. Jewell, J. G. Mangum, & J. Bally, 39–46
- Heald, G., Józsa, G., Serra, P., et al. 2011, *A&A*, 526, A118
- Henry, R. B. C. & Worthey, G. 1999, *PASP*, 111, 919
- Hollenbach, D. J. & Thronson, Harley A., J., eds. 1987, *Astrophysics and Space Science Library*, Vol. 134, *Interstellar processes*
- Huchra, J. P., Macri, L. M., Masters, K. L., et al. 2012, *ApJS*, 199, 26
- Huchtmeier, W. K. 1982, *A&A*, 110, 121
- Irwin, J., Beck, R., Benjamin, R. A., et al. 2012, *AJ*, 144, 43
- Irwin, J., Beck, R., Cook, T., et al. 2024, *Galaxies*, 12, 22
- Irwin, J., Wiegert, T., Merritt, A., et al. 2019, *AJ*, 158, 21
- Irwin, J. A., Henriksen, R. N., Krause, M., et al. 2015, *ApJ*, 809, 172
- Irwin, J. A., Schmidt, P., Damas-Segovia, A., et al. 2017, *MNRAS*, 464, 1333
- Irwin, J. A. & Sofue, Y. 1992, *ApJ*, 396, L75
- Israel, F. P. 2009a, *A&A*, 493, 525
- Israel, F. P. 2009b, *A&A*, 506, 689
- Jiang, Y., Li, J.-T., Gao, Y., et al. 2024, *MNRAS*, 528, 4160
- Jiménez-Donaire, M. J., Cormier, D., Bigiel, F., et al. 2017, *ApJ*, 836, L29
- Kennicutt, Robert C., J. 1998, *ApJ*, 498, 541
- Kennicutt, R. C. & Evans, N. J. 2012, *ARA&A*, 50, 531
- Krause, M., Irwin, J., Wiegert, T., et al. 2018, *A&A*, 611, A72
- Krumholz, M. R., McKee, C. F., & Tumlinson, J. 2009, *ApJ*, 693, 216

- Leroy, A., Bolatto, A. D., Simon, J. D., & Blitz, L. 2005, *ApJ*, 625, 763
- Leroy, A. K., Rosolowsky, E., Usero, A., et al. 2022, *ApJ*, 927, 149
- Leroy, A. K., Walter, F., Bigiel, F., et al. 2009, *AJ*, 137, 4670
- Leroy, A. K., Walter, F., Brinks, E., et al. 2008, *AJ*, 136, 2782
- Leroy, A. K., Walter, F., Sandstrom, K., et al. 2013, *AJ*, 146, 19
- Li, J.-T., Beck, R., Dettmar, R.-J., et al. 2016a, *MNRAS*, 456, 1723
- Li, J.-T., Bregman, J. N., Wang, Q. D., Crain, R. A., & Anderson, M. E. 2016b, *ApJ*, 830, 134
- Li, J.-T., Bregman, J. N., Wang, Q. D., Crain, R. A., & Anderson, M. E. 2018, *ApJ*, 855, L24
- Li, J.-T., Bregman, J. N., Wang, Q. D., et al. 2017, *ApJS*, 233, 20
- Li, J.-T., Crain, R. A., & Wang, Q. D. 2014, *MNRAS*, 440, 859
- Li, J.-T., Lu, L.-Y., Qu, Z., et al. 2024, *ApJ*, 967, 78
- Li, J.-T. & Wang, Q. D. 2013a, *MNRAS*, 428, 2085
- Li, J.-T. & Wang, Q. D. 2013b, *MNRAS*, 435, 3071
- Li, J.-T., Zhou, P., Jiang, X., Bregman, J. N., & Gao, Y. 2019, *ApJ*, 877, 3
- Lisenfeld, U., Espada, D., Verdes-Montenegro, L., et al. 2011, *A&A*, 534, A102
- Lisenfeld, U., Ogle, P. M., Appleton, P. N., Jarrett, T. H., & Moncada-Cuadri, B. M. 2023, *A&A*, 673, A87
- Lisenfeld, U., Xu, C. K., Gao, Y., et al. 2019, *A&A*, 627, A107
- Lu, L.-Y., Li, J.-T., Vargas, C. J., et al. 2023, *MNRAS*, 519, 6098
- Lu, L.-Y., Li, J.-T., Vargas, C. J., et al. 2024, *arXiv e-prints*, arXiv:2410.02347
- Makarov, D., Prugniel, P., Terekhova, N., Courtois, H., & Vauglin, I. 2014, *A&A*, 570, A13
- McGaugh, S. S. 2005, *ApJ*, 632, 859
- McGaugh, S. S., Schombert, J. M., Bothun, G. D., & de Blok, W. J. G. 2000, *ApJ*, 533, L99
- Meier, D. S. & Turner, J. L. 2004, *AJ*, 127, 2069
- Paglione, T. A. D., Wall, W. F., Young, J. S., et al. 2001, *ApJS*, 135, 183
- Pan, H.-A., Lin, L., Hsieh, B.-C., et al. 2018, *ApJ*, 868, 132
- Papadopoulos, P. P. & Seaquist, E. R. 1999, *ApJ*, 516, 114
- Papadopoulos, P. P., van der Werf, P. P., Xilouris, E. M., et al. 2012, *MNRAS*, 426, 2601
- Peñaloza, C. H., Clark, P. C., Glover, S. C. O., & Klessen, R. S. 2018, *MNRAS*, 475, 1508
- Peñaloza, C. H., Clark, P. C., Glover, S. C. O., Shetty, R., & Klessen, R. S. 2017, *MNRAS*, 465, 2277
- Renaud, F., Bournaud, F., Kraljic, K., & Duc, P. A. 2014, *MNRAS*, 442, L33
- Roman-Duval, J., Heyer, M., Brunt, C. M., et al. 2016, *ApJ*, 818, 144
- Rosolowsky, E. & Leroy, A. 2006, *PASP*, 118, 590
- Saintonge, A. & Catinella, B. 2022, *ARA&A*, 60, 319
- Saintonge, A., Catinella, B., Tacconi, L. J., et al. 2017, *ApJS*, 233, 22
- Saintonge, A., Kauffmann, G., Wang, J., et al. 2011, *MNRAS*, 415, 61
- Salim, S., Rich, R. M., Charlot, S., et al. 2007, *ApJS*, 173, 267
- Sandstrom, K. M., Leroy, A. K., Walter, F., et al. 2013, *ApJ*, 777, 5
- Schmidt, M. 1959, *ApJ*, 129, 243
- Shetty, R., Glover, S. C., Dullemond, C. P., et al. 2011, *MNRAS*, 415, 3253
- Skrutskie, M. F., Cutri, R. M., Stiening, R., et al. 2006, *AJ*, 131, 1163
- Solomon, P. M., Rivolo, A. R., Barrett, J., & Yahil, A. 1987, *ApJ*, 319, 730
- Solomon, P. M., Scoville, N. Z., & Sanders, D. B. 1979, *ApJ*, 232, L89
- Strong, A. W. & Mattox, J. R. 1996, *A&A*, 308, L21
- Sutter, J. & Fadda, D. 2022, *ApJ*, 941, 47
- Tacconi, L. J., Genzel, R., & Sternberg, A. 2020, *ARA&A*, 58, 157
- Tan, Q.-H., Gao, Y., Zhang, Z.-Y., & Xia, X.-Y. 2011, *Research in Astronomy and Astrophysics*, 11, 787
- Tremonti, C. A., Heckman, T. M., Kauffmann, G., et al. 2004, *ApJ*, 613, 898
- Truran, J. W. 1977, in *Astrophysics and Space Science Library*, Vol. 67, CNO Isotopes in Astrophysics, ed. J. Audouze, 145
- Vargas, C. J., Mora-Partiarroyo, S. C., Schmidt, P., et al. 2018, *ApJ*, 853, 128
- Vargas, C. J., Walterbos, R. A. M., Rand, R. J., et al. 2019, *ApJ*, 881, 26
- Vila-Vilaro, B., Cepa, J., & Zabludoff, A. 2015, *ApJS*, 218, 28
- Walter, F., Brinks, E., de Blok, W. J. G., et al. 2008, *AJ*, 136, 2563
- Wang, J., Lin, X., Yang, D., et al. 2024, *arXiv e-prints*, arXiv:2404.09422
- Wang, J., Yang, D., Oh, S. H., et al. 2023, *ApJ*, 944, 102
- Werk, J. K., Prochaska, J. X., Tumlinson, J., et al. 2014, *ApJ*, 792, 8
- Wiegert, T., Irwin, J., Miskolczi, A., et al. 2015, *AJ*, 150, 81
- Wilson, T. L., Rohlfs, K., & Hüttemeister, S. 2013, *Tools of Radio Astronomy*
- Wong, T. & Blitz, L. 2002, *ApJ*, 569, 157
- Xu, X., Wang, J., Li, Z., & Chen, Y. 2024, *ApJ*, 971, 165
- Yajima, Y., Sorai, K., Miyamoto, Y., et al. 2021, *PASJ*, 73, 257
- Yao, L., Seaquist, E. R., Kuno, N., & Dunne, L. 2003, *ApJ*, 588, 771
- Yim, K., Wong, T., Howk, J. C., & van der Hulst, J. M. 2011, *AJ*, 141, 48
- Young, J. S. & Knezek, P. M. 1989, *ApJ*, 347, L55
- Zanchettin, M. V., Feruglio, C., Massardi, M., et al. 2023, *A&A*, 679, A88
- Zheng, Y., Wang, J., Irwin, J., et al. 2022, *MNRAS*, 513, 1329